The lattice Boltzmann based large eddy simulations for the stenosis of the aorta

Xiao Xue[1], Jon W. S. McCullough[1], Sharp C. Y. Lo[1], Ioannis Zacharoudiou[1], Bálint Joó[4], and Peter V. Coveney[1,2,3]

[1] Centre for Computational Science, Department of Chemistry, University College London, London, UK
[2] Advanced Research Computing Centre, University College London, London, UK
[3] Informatics Institute, Faculty of Science, University of Amsterdam, Amsterdam, Netherlands
[4] Oak Ridge National Laboratory, Oak Ridge, TN, USA
x.xue@ucl.ac.uk

Abstract. Large eddy simulations (LES) are extensively employed in aerodynamics-related industrial research and applications. However, the application of lattice Boltzmann based LES techniques in vascular blood flow research is less extensively documented. This study investigates the feasibility of employing lattice Boltzmann based large eddy simulation techniques, specifically the Smagorinsky-based subgrid scale turbulence model, for simulating high Reynolds number blood flow at a coarse-grained resolution. Initially, a stenotic channel flow simulation is conducted, with results undergoing validation against existing experimental data and direct numerical simulation results, showing strong agreement for both. Subsequently, our model is applied to simulate aortic stenosis at a resolution of $100\mu m$, demonstrating the capability to model high Reynolds numbers around 4500, despite such flows conventionally requiring a resolution of around $20\mu m$. These results underscore the substantial promise of utilising LES techniques in blood flow simulations, benefiting not just the lattice Boltzmann method but also enlightening the broader computational fluid dynamics community. This approach offers advantages for large-scale human simulations at coarser resolutions.

Keywords: Large-eddy simulations · lattice Boltzmann method · turbulent flow · stenosis of the aorta

1 Introduction

Computational fluid dynamics (CFD) is vital for industrial applications ranging from physics, and engineering to biomedical applications. Direct numerical simulation (DNS) is directly solving the Navier-Stokes equations on a discretised domain by using finite-difference[32], finite-volume [9] and finite-element methods [44]. Despite high accuracy for CFD related problems, DNS is normally time-consuming and computationally expensive. Large-eddy simulations (LES) [30,31] can reduce the computational cost by modeling the subgrid-scale

ICCS Camera Ready Version 2024
To cite this paper please use the final published version:
DOI: 10.1007/978-3-031-63775-9_30

(SGS) turbulence. However, efficient LES calculations still suffer from the data-dependencies in their implementation and need refined grids [4,7,41] near the wall to correctly model the physics. To mitigate grid dependencies in LES-based simulations, coupling with RANS simulations near the wall is necessary [28]; however, this introduces additional coupling efforts.

The lattice Boltzmann method (LBM) [33] may be considered an alternative approach to solve some CFD problems numerically. Instead of solving the Navier-Stokes equations directly, LBM discretises the Boltzmann equation and implements the streaming and collision of probability density functions. Under limits imposed by a Chapman-Enskog analysis, LBM can be considered as an equivalent representation of solving the Navier-Stokes equations directly. Due to the inherent locality of the method, the LBM is relatively easy to deploy in parallel computing approaches compared to other conventional CFD methods. LBM has gained in popularity over the last few decades and has been successfully applied to various phenomena ranging from micro-nano fluidics problems [38,36,37,6], mesoscopic problems like blood flow simulations [42,12,25], and macroscopic scale problems [15,16,20,27]. In addition to its efficient parallelisation, the LBM is also suitable for sparsely configured complex geometry problems, namely blood fluid simulations [19] and flow through porous media [14].

HemeLB[22], is an LBM-based, open-source software package that is designed to study the sparse fluid domains characteristic of vascular geometries. The code is available in the repository [34]. In many hemodynamics studies using the LBM, the flows examined are often based on a relatively low Reynolds (Re) number ($Re < 1000$). Examples in the literature include those examining the circle of Willis [23], arteriovenous fistula [24] or aortic aneurysm [2]. From a physiological perspective however, previous studies have demonstrated that arterial blood flow can attain much higher Reynolds numbers (exceeding 4000 in some regions) [3]. Simulating this can be a challenge and such regimes can lead to utilising high resolution discretisations of the domain and can decrease the stability of the simulation [10]. Hou et al. [15] integrated the Smagorinsky Subgrid Scale (SGS) model into lattice Boltzmann frameworks by incorporating a turbulent effective viscosity, thereby marrying the relaxed resolution requirements of LES techniques with the efficient parallelisation of the LBM. LBM-based LES simulations are extensively employed for modeling turbulent flows [26,39,40], with applications spanning various industries. Notably, these simulations have been applied in the analysis of airfoils [5,29] and vehicle aerodynamics [11]. Conventionally, CFD modelling of turbulent aortic flow can result in significant computational costs, primarily due to the necessity of a fine grid near the vascular wall. [10,21,43].However, to the authors' knowledge, the application of lattice Boltzmann based LES methods in modelling blood flow simulations remains scarcely explored. In this study, we incorporate the Smagorinsky SGS model into the HemeLB solver, demonstrating the feasibility of employing a "coarse-grained" thoracic aorta model with a resolution of 100 μm, achieving results comparable to those at a 20 μm resolution [10].

ICCS Camera Ready Version 2024
To cite this paper please use the final published version:
DOI: 10.1007/978-3-031-63775-9_30

The structure of this paper is as follows: we elucidate the lattice Boltzmann method, inclusive of the subgrid scale turbulence model, applied to the hemodynamics solver [22], in Section 2. In Section 3, we initially assess the accuracy of the current LES model through a comparison with experimental data [8] and a DNS benchmark [17]. Subsequently, we contrast the stenosis in aortic flow with and without the incorporation of the turbulence model. Finally we summarize our findings and conclude in Section 4.

2 Methods

2.1 The lattice Boltzmann method

This study employs a three-dimensional (3D) Lattice Boltzmann model featuring 19 discretised directions, known as the D3Q19 model. The lattice cell is specified by its position $\mathbf{x}$ and time t, and is characterized by a discretised velocity set $\mathbf{c}_i$ where $i \in \{0, 1, \ldots, Q-1\}$ with $Q = 19$. The evolution equation for the distribution functions can be written as:

$$\mathbf{f}(\mathbf{x} + \mathbf{c}_i \Delta t, t + \Delta t) = \mathbf{f}(\mathbf{x}, t) - \mathbf{\Omega} \left[\mathbf{f}(\mathbf{x}, t) - \mathbf{f}^{eq}(\mathbf{x}, t) \right], \tag{1}$$

where $\mathbf{\Omega}$ denotes the Bhatnagar-Gross-Krook (BGK) or single relaxation time (SRT) collision kernel, defined as $\mathbf{\Omega} = \frac{\Delta t}{\tau}$ [33]. τ is the relaxation time. The collision kernel relaxes the distribution function towards the local Maxwellian distribution function f_i^{eq}:

$$f_i^{eq}(\mathbf{x}, t) = w_i \rho(\mathbf{x}, t) \left[1 + \frac{\mathbf{c}_i \cdot \mathbf{u}(\mathbf{x}, t)}{c_s^2} + \frac{\left[\mathbf{c}_i \cdot \mathbf{u}(\mathbf{x}, t) \right]^2}{2c_s^4} - \frac{\left[\mathbf{u}(\mathbf{x}, t) \cdot \mathbf{u}(\mathbf{x}, t) \right]}{2c_s^2} \right], \tag{2}$$

where w_i denotes the direction based weights ($w_i = 1/3$ for i=0, $1/18$ for the six nearest neighbours and $1/36$ for the remaining directions), $\rho(\mathbf{x}, t)$ is the cell macroscopic density, $\mathbf{u}(\mathbf{x}, t)$ is the cell macroscopic velocity. In Eq. (1), Δt symbolizes the lattice Boltzmann time step, which is set to unity. The LBM kinematic viscosity ν is defined as

$$\nu = c_s^2 \left(\tau - \frac{1}{2} \right) \Delta t, \tag{3}$$

with c_s representing the speed of sound, and c_s^2 equating to $1/3$ in Lattice Boltzmann Units (LBU). Macro-scale quantities such as density and momentum are derived from the moments of the distribution function $f_i(\mathbf{x}, t)$, the discrete velocities $\mathbf{c}_i$:

$$\rho(\mathbf{x}, t) = \sum_{i=0}^{Q-1} f_i(\mathbf{x}, t), \tag{4}$$

$$\rho(\mathbf{x}, t)\mathbf{u}(\mathbf{x}, t) = \sum_{i=0}^{Q-1} f_i(\mathbf{x}, t)\mathbf{c}_i, \tag{5}$$

ICCS Camera Ready Version 2024
To cite this paper please use the final published version:
DOI: 10.1007/978-3-031-63775-9_30

2.2 Smagorinsky subgrid-scale modelling

We now summarize the lattice Boltzmann based Smagorinsky SGS LES technique: Within the LBM framework, the effective viscosity ν_{eff} [30,15,18] is modelled as the sum of the molecular viscosity, ν_0, and the turbulent viscosity, ν_t:

$$\nu_{\text{eff}} = \nu_0 + \nu_t, \qquad \nu_t = C_{\text{smag}} \Delta^2 \left|\bar{\mathbf{S}}\right|, \tag{6}$$

where $\left|\bar{\mathbf{S}}\right|$ is the filtered strain rate tensor, C_{smag} is the Smagorinsky constant, Δ represents the filter size. We apply Eq. (6) into Eq. (3) to add the turbulent viscosity. The detailed demonstration of the turbulent viscosity can be found in [15,39].

2.3 Sponge layer implementation

To reduce the velocity fluctuations near the outlet, a *sponge zone* is set up as a damping region [13,1,39,40]. In the sponge zone, we impose a higher kinematic viscosity, ν_s, defined as

$$\nu_s = \nu_{\text{eff}} \left[1 + (p-1)\left(\frac{\|d\|}{w_{\text{width}}}\right)^2\right], \tag{7}$$

where p are empirical viscocity ratio constants which are set to $p = 1000$ in this work. $\|d\|$ denotes the distance of the lattice cell point to the outlet plane. w_{width} represents the width of the sponge zone prior to the outlet.

3 Results

In this section, we initially present the configuration of stenosis in turbulent channel flow for validation purposes, and subsequently conduct a comparative analysis with both experimental Particle Image Velocimetry (PIV) (Ding et al.) [8] and DNS datasets [17]. Subsequently, the potential of the LBM-based LES (LBM-LES) approach is elaborated upon, demonstrating its capability to simulate aortic flow at a resolution of $100\mu m$, which is coarser than the resolution attainable with the exclusive use of the BGK collision operator.

3.1 Validation of the turbulent channel flow simulation

As a validation exercise for the method, we first consider a high-resolution stenotic channel flow simulation. As depicted in Fig. 1, the dimensions of the stenotic channel flow are configured as $L_x \times L_y \times L_z$, where $L_x = 266\delta$, $L_y = 22\delta$, and $L_z = 2\delta$ correspond to the streamwise, spanwise, and vertical directions, respectively. Here, δ denotes the turbulent boundary layer thickness, set at $\delta = 0.0045m$. The lattice resolution is set to $100\mu m$, resulting in a simulation domain composed of approximately 1.0×10^9 lattice cells. The Smagorinsky constant is set to $C_{\text{smag}} = 0.01$ in this simulation. The domain is driven by an inlet

ICCS Camera Ready Version 2024
To cite this paper please use the final published version:
DOI: 10.1007/978-3-031-63775-9_30

boundary condition characterized by a plug velocity profile, where the maximum velocity reaches $2.16m/s$. The outlet is configured with a pressure-free boundary condition to facilitate flow egress without additional resistance. To enhance the stability, a sponge zone, highlighted in the figure in orange, is positioned prior to the outlet to absorb reflective waves triggered by non-equilibrium bounce-back effects at the outlet. The sponge zone is set to 4δ to ensure the stability of the simulation. Both the upper and lower planes in the z direction are assigned no-slip boundary conditions. Unlinke the setups described in other studies [18,39],

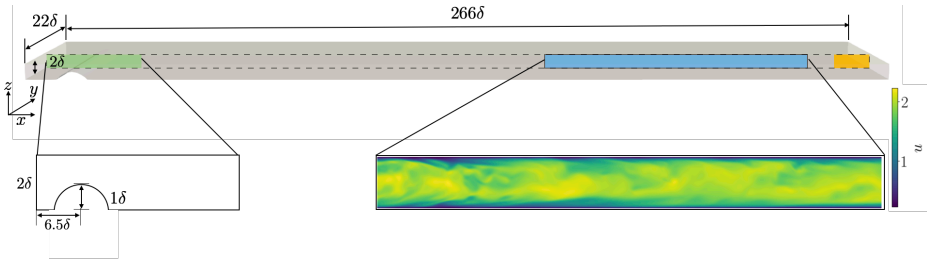

Fig. 1: Illustration of a stenotic channel flow simulation setup: The depicted stenotic channel commences with a semi-cylindrical bump, possessing a height of 1δ, obstructing 50% of the channel's cross-section. The green zone demonstrates the semi-cylindrical obstacle's configuration. The blue zone shows a snapshot where the channel flow has evolved into a fully developed turbulent velocity profile. The orange zone represents the sponge zone, designed to absorb reflective waves emanating from the outlet.

periodic boundary conditions are not employed in the spanwise direction. Instead, a wide channel with no-slip boundary conditions, mirroring the experimental configurations [8], is implemented. To accelerate the turbulent transition adaptation length, a semi-cylindrical obstacle with the height of a half-sphere is positioned at 6.5δ from the inlet. Initially, the inlet flow is established as laminar, but the presence of the obstacle disrupts the flow's symmetry, leading to a gradual transition to turbulent flow. The inlet velocity is incrementally increased from $0.1m/s$ to $2.16m/s$ over a duration of 1 second. The computational cost for running the validation case can be find in Tab 1

Computational model	CPU type	number of cores	Timesteps
Stenotic channel flow	AMD EPYC Zen2	8192	2,000,000
Aortic flow	AMD EPYC Zen2	8192	2,500,000

Table 1: Table for the computational time for both stenotic channel flow validation and stenotic aortic flow simulation.

ICCS Camera Ready Version 2024
To cite this paper please use the final published version:
DOI: 10.1007/978-3-031-63775-9_30

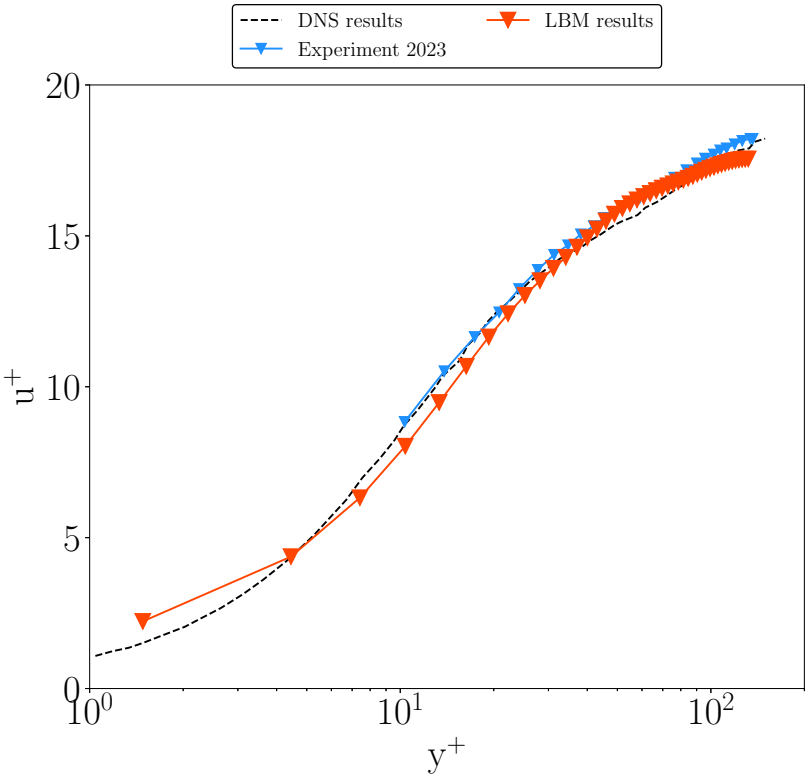

Fig. 2: Representation of u^+ as a function of y^+, where the black dotted line illustrates the DNS reference data [17]. The blue triangles depict the PIV experiment data from Ding et al.[8]. The red triangles represent the data obtained from our LBM-LES simulation.

Upon reaching the maximum velocity, the simulation continues for an additional second to ensure that the turbulent flow fully develops. The channel flow simulation yields a Reynolds number, Re, approximately equal to 4600. Simultaneously, the friction Reynolds number, Re_τ, is estimated to be around 130. The expressions defining Re and Re_τ are presented as

$$Re = u_{\max} * H/\nu, \qquad Re_\tau = u_\tau * H/\nu \tag{8}$$

where Re is characterized by the maximum velocity and Re_τ is measured by the shear velocity. H is the channel flow height which is $9 \times 10^{-3} m$, ν is the kinematic viscosity which is set to $4 \times 10^{-6} m^2/s$. We commence collecting statistics after the first second of simulation, focusing on the blue region illustrated in Fig. 1, positioned at the channel's mid cross-section, extending from $0.2m$ to $0.4m$. The spatial ensemble average of the streamwise velocity, u^+, as a function of y^+, is calculated. These variables represent the dimensionless mean velocity and the

ICCS Camera Ready Version 2024
To cite this paper please use the final published version:
DOI: 10.1007/978-3-031-63775-9_30

dimensionless distance from the wall, respectively, offering insights into the flow characteristics within the specified region.

$$u^+ = \frac{\langle u \rangle}{u_\tau}, \qquad y^+ = y\frac{\sqrt{\tau_\omega/\rho}}{\nu}, \tag{9}$$

where $\langle \cdot \rangle$ denotes the ensemble average over the streamwise direction. u represents the streamwise velocity, and u_τ is defined as the shear velocity. The variable y denotes the physical distance to the wall, while τ_w represents the wall shear stress. ν is the kinematic viscosity from the LBM simulation obtained via Eq. (3). As depicted in Fig. 2, the experimental data begins from $y^+ = 10$, whereas the y^+ for the first cell near the wall in the LBM-LES simulation is approximately $y^+ = 1.5$. Although there is a minor deviation in the first cell, the LBM-LES simulation aligns well with both experimental and DNS references. For $y^+ > 30$, the LBM-LES results deviate slightly from the DNS data but remain in close agreement with the experimental results. Overall, the LBM-LES implementation demonstrates good concordance with both experimental and DNS simulations.

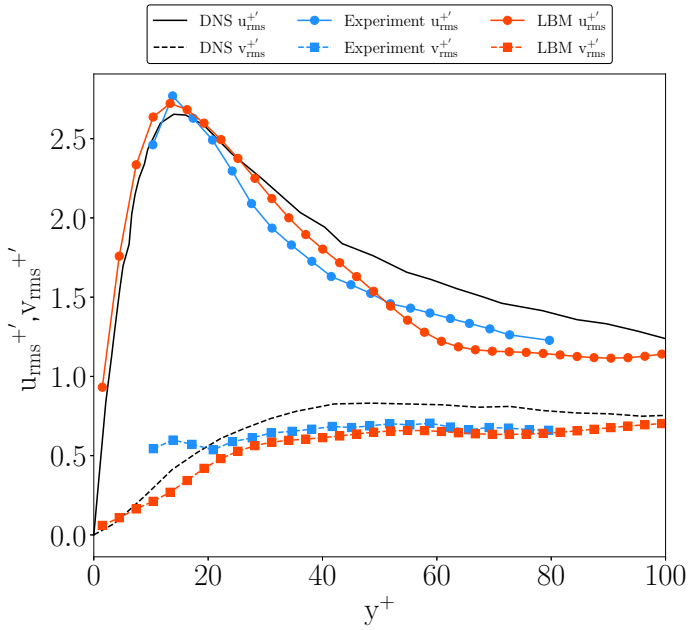

Fig. 3: Presentation of $u_{rms}{}^{+\prime}$ and $v_{rms}{}^{+\prime}$ as functions of y^+, with the black and black dotted lines representing the DNS reference data [17]. The blue circles and squares correspond to $u_{rms}{}^{+\prime}$ and $v_{rms}{}^{+\prime}$ from the experiment results [8], respectively. Additionally, the red circles and squares depict the LBM simulation outcomes for $u_{rms}{}^{+\prime}$ and $v_{rms}{}^{+\prime}$, respectively.

ICCS Camera Ready Version 2024
To cite this paper please use the final published version:
DOI: 10.1007/978-3-031-63775-9_30

Furthermore, we examined the dimensionless root mean square (RMS) for two velocity components on streamwise and vertical direction. $\mathrm{u}^{+\prime}_{\mathrm{rms}}$, $\mathrm{v}^{+\prime}_{\mathrm{rms}}$ are the dimensionless RMS velocity components that are normalized with the shear velocity u_τ:

$$\mathrm{u}^{+\prime}_{\mathrm{rms}} = \frac{\sqrt{(u(\mathbf{x}) - \langle u \rangle)^2}}{u_\tau}. \tag{10}$$

Spatial averaging for RMS is performed only during post-processing due to the high resolution of the simulation. In Fig. 3, the red markers represent the LBM-LES simulation results, while the blue markers correspond to the PIV experimental reference, and the black lines denote the DNS reference. Both experimental and LBM-LES results successfully capture the peak value of $u^{+\prime}_{\mathrm{rms}}$ compared with the DNS data. Beyond the peak, both LBM-LES and experimental results gradually deviate from the DNS data, which may be attributed to statistical issues and the confinement of the channel flow in the spanwise direction. Regarding the vertical velocity component $u^{+\prime}_{\mathrm{rms}}$, LBM-LES results align well with the experimental data but are slightly lower than the DNS results for $y^+ > 20$.

Considering both Fig. 2 and Fig. 3, it is evident that the LBM-LES implementation aligns closely with experimental and DNS results, demonstrating its capability to capture turbulent statistical quantities accurately. The comparison reveals that the LBM-LES method effectively replicates the key features of turbulent flows, confirming its reliability in modeling complex flow dynamics. This alignment shows the potential of LBM-LES in contributing valuable insights into the understanding of turbulence, particularly in the context of fluid dynamics simulations.

3.2 Simulation of high Reynolds number flow in a stenosis of the aorta

In this subsection, we present our capability to simulate blood flow at $Re = 4500$ utilising our LBM-LES methodology. Specifically, we apply this technique to simulate stenotic blood flow within a thoracic aorta model [35], which has an inlet diameter of approximately $0.01m$. The largest lattice spacing required to reasonbly represent such a domain is approximately $100\mu m$. However, the BGK collision operator faces challenges in achieving stable simulations at this resolution (especially at elevated Re) due to the limited choice of the relaxation time τ. For a reliable simulation of stenotic aorta flow, a finer resolution of $20\mu m$ for the geometry may be necessary. To illustrate the benefit of LES techniques, we set to the model resolution in our study to $100\mu m$ with the Smagorinsky constant set to $C_{\mathrm{smag}} = 0.01$. As a proof of the concept, the model is initialized with an inlet velocity around $1m/s$. Pressure-free outlet conditions are established for three branches leading to the cerebral and upper limb vasculature and a singular outlet in the bottom leading to the descending aorta. The sponge regions are set near the outlets of the vascular with $p = 1000$ in Eq. (7). As shown in Fig. 4, the LBM-LES based simulation is able to capture the pressure drop due to the presence of the nearing part of the aorta. The cross-sectional views on upper, middle,

ICCS Camera Ready Version 2024
To cite this paper please use the final published version:
DOI: 10.1007/978-3-031-63775-9_30

and lower section near the aortic constriction shows that on the upper plane, the mean velocity is around $1m/s$, the reduced cross-section of the middle section leads to the acceleration of the blood flow to around $1.8m/s$. Furthermore, the high blood flow velocity leads to turbulent flow in the lower part of the stenotic region. The presence of the blockage will also lead to a pressure drop [10] which is observed in our simulation. We emphasise that the typical resolution for the stenotic aorta would be around $20\mu m$ resolution, whereas, our configuration is able to observe similar velocity and pressure profile at $100\mu m$ resolution. The computational cost for running the stenotic aorta flow is illustrated in Tab 1

Fig. 5 provides an instantaneous snapshot illustrating the surface stress profile

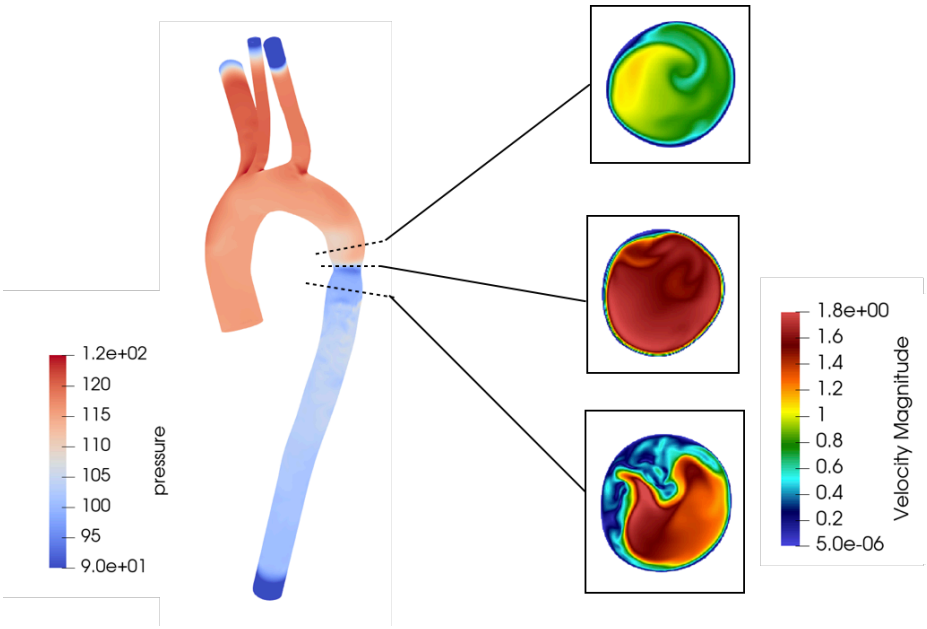

Fig. 4: Instantaneous snapshot of aortic stenosis simulation: on the left-hand side, the pressure distribution within the aortic flow is depicted. The right-hand side illustrates three cross-sectional views—upper, middle, and lower—proximal to the aortic constriction. This figure effectively demonstrates the capability of HemeLB to capture the blood flow behavior of aortic flow at a stenotic location with a maximum velocity of $1.8m/s$.

of the aorta, along with the velocity profile across a section near the stenotic region. This figure highlights that the area proximal to the aortic constriction exhibits significantly elevated wall shear stress, indicative of the stenosis acting as an obstruction, impeding blood flow and directing it towards the descending aorta. Consequently, the upper region of the aorta is subjected to increased blood pressure, as depicted in Fig. 4. Elevated wall shear stress is also observed near

ICCS Camera Ready Version 2024
To cite this paper please use the final published version:
DOI: 10.1007/978-3-031-63775-9_30

the aortic outlets, attributed to the implementation of the sponge layer. On the right-hand side of Fig. 5, the velocity profile within the aorta is presented, revealing a laminar-turbulent transition induced by aortic stenosis. Mirroring the stenotic channel flow simulation illustrated in Fig. 1, the flow evolves into a turbulent state, achieving a peak velocity of approximately $1.8m/s$. This transition underscores the complexity of flow patterns in the areas of aortic constriction, reflecting the significant impact of stenosis on the hemodynamic behavior of the aorta.

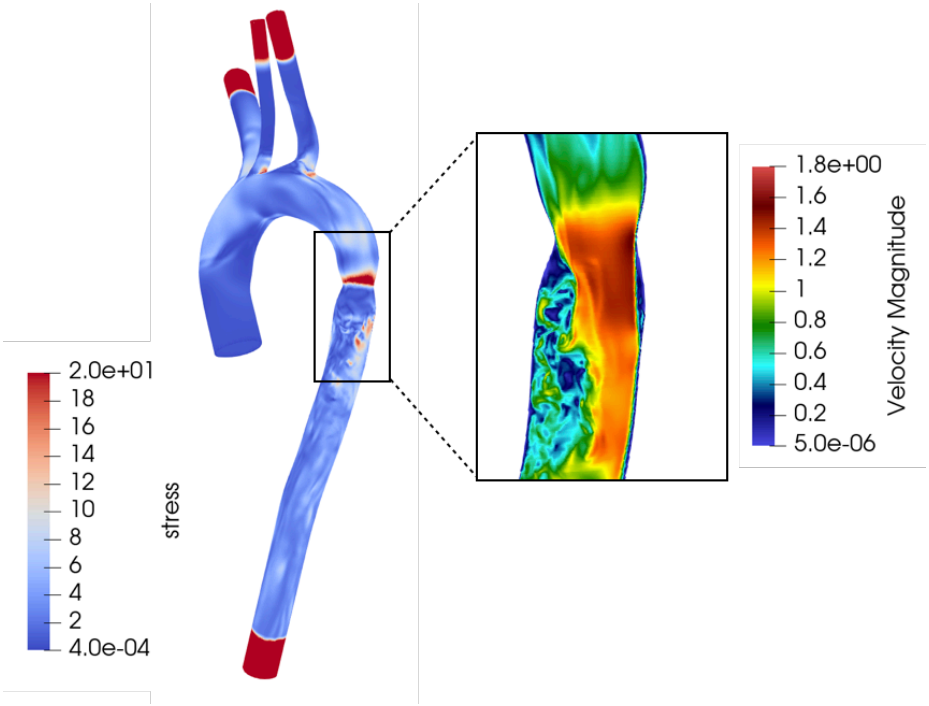

Fig. 5: The snapshot presents an instantaneous simulation of wall shear stress in stenotic aortic flow, featuring a cross-sectional visualization near the region of aortic stenosis. The velocity magnitude profile within this cross-section highlights the transition from laminar to turbulent flow, a phenomenon occurring within the stenotic segment of the aorta.

4 Conclusion

In this study, the integration of the Smagorinsky turbulence model into the HemeLB framework is evaluated for simulating high Reynolds number aortic flow. The validation involved a high-resolution stenotic channel flow, showcasing

ICCS Camera Ready Version 2024
To cite this paper please use the final published version:
DOI: 10.1007/978-3-031-63775-9_30

the laminar-turbulent transition along the streamwise direction. Quantitative analysis is conducted at a downstream cross-section located at $y = 11\delta$, where the flow transitions to full turbulence. Here, both the mean velocity profile and the RMS values of the streamwise and vertical velocities exhibited good agreement with experimental and DNS reference data. The LBM-LES methodology is then applied to aortic stenosis flow simulations, utilising a sponge layer and turbulence model to qualitatively replicate the phenomenological behavior observed in aortic stenosis, including increased blood pressure in the upper part of the stenotic region, high shear-stress near the region, and the occurrence of laminar-turbulent transition within the stenotic segment of the aorta. This work underscores the fact that the simulations of stenotic aorta can be conducted at a resolution of $100\mu m$, whereas standard simulations typically require a finer resolution of $20\mu m$ [10]. Future efforts will focus on an in-depth quantitative analysis of the aortic stenotic flow simulation. utilising the current technique could pave the way for full human simulation, making comprehensive computational modeling more feasible and realistic.

5 Acknowledgements

We acknowledge funding support from European Commission CompBioMed Centre of Excellence (Grant No. 675451 and 823712). Support from the UK Engineering and Physical Sciences Research Council under the projects “UK Consortium on Mesoscale Engineering Sciences (UKCOMES)" (Grant No. EP/R029598/1) and “Software Environment for Actionable and VVUQ-evaluated Exascale Applications (SEAVEA)" (Grant No. EP/W007711/1) is gratefully acknowledged. This research used resources of the Oak Ridge Leadership Computing Facility at the Oak Ridge National Laboratory, which is supported by the Office of Science of the U.S. Department of Energy under Contract No. DE-AC05-00OR22725.

References

1. Adams, N.A.: Direct numerical simulation of turbulent compression ramp flow. Theoretical and Computational Fluid Dynamics **12**(2), 109–129 (1998)
2. Afrouzi, H.H., Ahmadian, M., Hosseini, M., Arasteh, H., Toghraie, D., Rostami, S.: Simulation of blood flow in arteries with aneurysm: Lattice boltzmann approach (lbm). Computer methods and programs in biomedicine **187**, 105312 (2020)
3. Axner, L., Hoekstra, A.G., Jeays, A., Lawford, P., Hose, R., Sloot, P.: Simulations of time harmonic blood flow in the mesenteric artery: comparing finite element and lattice boltzmann methods. Biomedical engineering online **8**(1), 1–8 (2009)
4. Chapman, D.R.: Computational aerodynamics development and outlook. AIAA journal **17**(12), 1293–1313 (1979)
5. Chen, X.P.: Applications of lattice boltzmann method to turbulent flow around two-dimensional airfoil. Engineering Applications of Computational Fluid Mechanics **6**(4), 572–580 (2012)
6. Chiappini, D., Xue, X., Falcucci, G., Sbragaglia, M.: Ligament break-up simulation through pseudo-potential lattice Boltzmann method. In: AIP Conference Proceedings. vol. 1978, p. 420003. AIP Publishing (2018)

ICCS Camera Ready Version 2024
To cite this paper please use the final published version:
DOI: 10.1007/978-3-031-63775-9_30

7. Choi, H., Moin, P.: Grid-point requirements for large eddy simulation: Chapman?s estimates revisited. Physics of Fluids **24**(1), 011702 (2012)
8. Ding, G., Choi, K.S., Ma, B., Kato, T., Yuan, W.: Transitional pulsatile flows with stenosis in a two-dimensional channel. Physics of Fluids **33**(3) (2021)
9. Eymard, R., Gallouët, T., Herbin, R.: Finite volume methods. Handbook of numerical analysis **7**, 713–1018 (2000)
10. Feiger, B., Gounley, J., Adler, D., Leopold, J.A., Draeger, E.W., Chaudhury, R., Ryan, J., Pathangey, G., Winarta, K., Frakes, D., et al.: Accelerating massively parallel hemodynamic models of coarctation of the aorta using neural networks. Scientific reports **10**(1), 9508 (2020)
11. Gaedtke, M., Wachter, S., Raedle, M., Nirschl, H., Krause, M.J.: Application of a lattice boltzmann method combined with a smagorinsky turbulence model to spatially resolved heat flux inside a refrigerated vehicle. Computers & Mathematics with Applications **76**(10), 2315–2329 (2018)
12. Groen, D., Richardson, R.A., Coy, R., Schiller, U.D., Chandrashekar, H., Robertson, F., Coveney, P.V.: Validation of patient-specific cerebral blood flow simulation using transcranial doppler measurements. Frontiers in physiology **9**, 721 (2018)
13. Guo, Y., Kleiser, L., Adams, N.: A comparison study of an improved temporal DNS and spatial DNS of compressible boundary layer transition. In: Fluid Dynamics Conference. p. 2371 (1994)
14. Han, Y., Cundall, P.A.: Lbm–dem modeling of fluid–solid interaction in porous media. International Journal for Numerical and Analytical Methods in Geomechanics **37**(10), 1391–1407 (2013)
15. Hou, S., Sterling, J., Chen, S., Doolen, G.: A lattice Boltzmann subgrid model for high Reynolds number flows. Pattern formation and lattice gas automata pp. 151–166 (1995)
16. Karlin, I.V., Ferrante, A., Öttinger, H.C.: Perfect entropy functions of the lattice Boltzmann method. EPL (Europhysics Letters) **47**(2), 182 (1999)
17. Kim, J., Moin, P., Moser, R.: Turbulence statistics in fully developed channel flow at low reynolds number. Journal of fluid mechanics **177**, 133–166 (1987)
18. Koda, Y., Lien, F.S.: The lattice Boltzmann method implemented on the gpu to simulate the turbulent flow over a square cylinder confined in a channel. Flow, Turbulence and Combustion **94**(3), 495–512 (2015)
19. Krüger, T., Holmes, D., Coveney, P.V.: Deformability-based red blood cell separation in deterministic lateral displacement devices?a simulation study. Biomicrofluidics **8**(5), 054114 (2014)
20. Lallemand, P., Luo, L.S.: Theory of the lattice Boltzmann method: Dispersion, dissipation, isotropy, Galilean invariance, and stability. Physical review E **61**(6), 6546 (2000)
21. Leuprecht, A., Kozerke, S., Boesiger, P., Perktold, K.: Blood flow in the human ascending aorta: a combined mri and cfd study. Journal of engineering mathematics **47**, 387–404 (2003)
22. Mazzeo, M.D., Coveney, P.V.: Hemelb: A high performance parallel lattice-boltzmann code for large scale fluid flow in complex geometries. Computer Physics Communications **178**(12), 894–914 (2008)
23. McCullough, J.W., Coveney, P.V.: High resolution simulation of basilar artery infarct and flow within the circle of willis (2023)
24. McCullough, J., Coveney, P.: High fidelity blood flow in a patient-specific arteriovenous fistula. Scientific Reports **11**(1), 22301 (2021)

ICCS Camera Ready Version 2024
To cite this paper please use the final published version:
DOI: 10.1007/978-3-031-63775-9_30

25. Nash, R.W., Carver, H.B., Bernabeu, M.O., Hetherington, J., Groen, D., Krüger, T., Coveney, P.V.: Choice of boundary condition for lattice-boltzmann simulation of moderate-reynolds-number flow in complex domains. Physical Review E **89**(2), 023303 (2014)
26. Sagaut, P.: Toward advanced subgrid models for lattice-boltzmann-based large-eddy simulation: Theoretical formulations. Computers & Mathematics with Applications **59**(7), 2194–2199 (2010)
27. Shao, X., Santasmasas, M.C., Xue, X., Niu, J., Davidson, L., Revell, A.J., Yao, H.D.: Near-wall modeling of forests for atmosphere boundary layers using lattice Boltzmann method on GPU. Engineering Applications of Computational Fluid Mechanics **16**(1), 2142–2155 (2022)
28. Shur, M.L., Spalart, P.R., Strelets, M.K., Travin, A.K.: Synthetic turbulence generators for RANS-LES interfaces in zonal simulations of aerodynamic and aeroacoustic problems. Flow, turbulence and combustion **93**(1), 63–92 (2014)
29. Si, H., Shi, Y.: Study on lattice boltzmann method/large eddy simulation and its application at high reynolds number flow. Advances in Mechanical Engineering **7**(3), 1687814015573829 (2015)
30. Smagorinsky, J.: General circulation experiments with the primitive equations: I. the basic experiment. Monthly Weather Review **91**(3), 99–164 (1963)
31. Spalart, P., Allmaras, S.: A one-equation turbulence model for aerodynamic flows. In: 30th aerospace sciences meeting and exhibit. p. 439 (1992)
32. Strikwerda, J.C.: Finite difference schemes and partial differential equations. SIAM (2004)
33. Succi, S.: The Lattice Boltzmann Equation for Fluid Dynamics and Beyond. Oxford University Press (2001)
34. UCL: Hemelb cpu code. `https://github.com/UCL-CCS/HemePure` (2008)
35. Wilson, N.M., Ortiz, A.K., Johnson, A.B.: The Vascular Model Repository: A Public Resource of Medical Imaging Data and Blood Flow Simulation Results. Journal of Medical Devices **7**(4) (12 2013). `https://doi.org/10.1115/1.4025983`, `https://doi.org/10.1115/1.4025983`
36. Xue, X., Biferale, L., Sbragaglia, M., Toschi, F.: A lattice Boltzmann study on Brownian diffusion and friction of a particle in a confined multicomponent fluid. Journal of Computational Science **47**, 101113 (2020)
37. Xue, X., Biferale, L., Sbragaglia, M., Toschi, F.: A lattice Boltzmann study of particle settling in a fluctuating multicomponent fluid under confinement. The European Physical Journal E **44**(11), 1–10 (2021)
38. Xue, X., Sbragaglia, M., Biferale, L., Toschi, F.: Effects of thermal fluctuations in the fragmentation of a nanoligament. Physical Review E **98**(1), 012802 (2018)
39. Xue, X., Yao, H.D., Davidson, L.: Synthetic turbulence generator for lattice Boltzmann method at the interface between RANS and LES. Physics of Fluids **34**(5), 055118 (2022)
40. Xue, X., Yao, H.D., Davidson, L.: Wall-modeled large-eddy simulation integrated with synthetic turbulence generator for multiple-relaxation-time lattice Boltzmann method. Physics of Fluids **35**(6), 065115 (2023)
41. Yang, X.I., Griffin, K.P.: Grid-point and time-step requirements for direct numerical simulation and large-eddy simulation. Physics of Fluids **33**(1), 015108 (2021)
42. Zacharoudiou, I., McCullough, J., Coveney, P.: Development and performance of a hemelb gpu code for human-scale blood flow simulation. Computer Physics Communications **282**, 108548 (2023)

ICCS Camera Ready Version 2024
To cite this paper please use the final published version:
DOI: 10.1007/978-3-031-63775-9_30

43. Zakaria, M.S., Ismail, F., Tamagawa, M., Azi, A.F.A., Wiriadidjaya, S., Basri, A.A., Ahmad, K.A.: Computational fluid dynamics study of blood flow in aorta using openfoam. Journal of Advanced Research in Fluid Mechanics and Thermal Sciences **43**(1), 81–89 (2018)
44. Zienkiewicz, O.C., Taylor, R.L., Zhu, J.Z.: The finite element method: its basis and fundamentals. Elsevier (2005)

ICCS Camera Ready Version 2024
To cite this paper please use the final published version:
DOI: 10.1007/978-3-031-63775-9_30